International Journal of Fatigue 141 (2020) 105856

Contents lists available at ScienceDirect

International Journal of Fatigue

journal homepage: www.elsevier.com/locate/ijfatigue

Fatigue behavior and modeling for additive manufactured 304L stainless steel: The effect of surface roughness

Seungjong Lee[a,b], Jonathan W. Pegues[b,c], Nima Shamsaei[a,b,*]

[a] Department of Mechanical Engineering, Auburn University, Auburn, AL 36849, USA
[b] National Center for Additive Manufacturing Excellence (NCAME), Auburn University, Auburn, AL 36849, USA
[c] Material, Physical, and Chemical Sciences Center, Sandia National Laboratories, Albuquerque, NM 87185, USA

ARTICLE INFO

Keywords:
Laser beam powder bed fusion (LB-PBF)
Surface topology
Stainless steel
Fatigue behavior
Fatigue life estimation

ABSTRACT

The fatigue strength of additively manufactured metallic parts in their as-built surface condition is mainly dominated by the surface roughness. Post-processing is often inevitable to reduce surface roughness effects even though post-processing diminishes the main advantage of additive manufacturing, which is net-shaped direct-to-service production. This study investigates the underlying mechanisms responsible for fatigue failure of additively manufactured 304L stainless steel parts in as-built and machined/polished surface conditions. Both strain- and force-controlled, fully reversed fatigue tests were conducted to gain a comprehensive understanding of surface roughness effects on fatigue behavior. The sensitivity to surface roughness is shown to be dependent on the control mode, with stress-based fatigue tests showing greater sensitivity than strain-based fatigue tests. Moreover, the fatigue life estimation for as-built specimens was performed based on surface roughness parameters as well as the fatigue properties of the specimens in machined/polished surface condition of the material without using any fatigue data of specimens in as-built surface condition. Accordingly, the effect of surface roughness on the fatigue behavior could be estimated reasonably well in both strain-life and stress-life approaches.

1. Introduction

Metallic additive manufacturing (AM) has been recognized as notable technology for its ability to produce complex and/or customized components without additional efforts including tooling or machining processes [1]. Complex production processes such as simultaneous fabrication of several components into a single part can be performed within the AM machine, making additional assembly processes unnecessary. In addition, AM enables users to produce parts with complex geometries such as lattice and porous structures unobtainable through conventional subtractive processes. Moreover, AM is more capable of providing small quantity production, without the excessive tooling costs that limit this type of production in traditional manufacturing techniques. For example, aerospace and biomedical industries can reduce costs and lead times associated with small-batch, legacy, or custom components, using AM. Consequently, AM has been studied and reviewed by a number of researchers to better understand and improve the quality and reliability of manufactured products [1–8].

One of the major advantages of using AM is that parts can be fabricated to net shape and directly implemented into service without additional processing steps. However, the surface roughness (SR) that is typical for additively manufactured parts in as-built (AB) surface condition has proven to be extremely detrimental to their fatigue resistance [8–15]. The SR is caused and affected by several processing characteristics of AM technology; i.e. process parameters, unmelted/partially-melted powder particles on the surface, layer-wise processing nature of AM, stair-step effects (build orientation), the geometry of the parts, etc. [16]. Therefore, many studies have investigated the correlation between fatigue performance and SR [16–22], including attempts to elucidate the critical SR parameters most representative for the SR effect on the fatigue behavior [23–26]. To date, however, no consensus has been established regarding the most informative SR parameter with many of the works being in disagreement.

As a representative of SR values, R_a, provides the general context of average surface topography. The surface, which has a higher R_a value, is believed to introduce higher stress concentrations and lower fatigue resistance. Therefore, most research works regarding fatigue behavior have used this representative SR value [27–29]. However, R_a may not fully capture the critical geometry effects related to the micro-notches affecting the fatigue crack initiation process [30]. Therefore, some

* Corresponding author at: Department of Mechanical Engineering, Auburn University, Auburn, AL 36849, USA.
E-mail address: shamsaei@auburn.edu (N. Shamsaei).

https://doi.org/10.1016/j.ijfatigue.2020.105856
Received 16 June 2020; Received in revised form 21 July 2020; Accepted 24 July 2020
Available online 28 July 2020

Nomenclature

b	Fatigue strength exponent
b'	Estimated fatigue strength exponent
c	Fatigue ductility exponent
E	Modulus of elasticity
f	Fatigue strength fraction factor
K'	Cyclic strength coefficient
$\bar{K}_t$	Effective elastic stress concentration factor
$\bar{K}_f$	Effective fatigue notch factor
n	Stress state
n'	Cyclic strain hardening exponent
N	Number of cycles
$2N_f$	Reversals to failure
q	Notch sensitivity of the material
R_a	Arithmetical mean height of the profiled line
R_t	Maximum peak-to-valley height of the profiled line
R_v	Maximum valley height of the profiled line
R_{zISO}	10-point height roughness of the profiled line
ε_a	Strain amplitude
ε_f'	Fatigue ductility coefficient
$\frac{\Delta\varepsilon_e}{2}$	Elastic strain amplitude
$\frac{\Delta\varepsilon_p}{2}$	Plastic strain amplitude
$\varepsilon_{p,acc}$	Accumulated plastic strain
γ	Material characteristic length
$\bar{\rho}_{10}$	10-point valley radii
σ_a	Stress amplitude
σ_f'	Fatigue strength coefficient
σ_m	Mean stress

Abbreviations

AB	As-built surface condition
AM	Additive manufacturing
DIMT	Deformation induced martensite transformation
HCF	High cycle fatigue
ICF	Intermediate cycle fatigue
LB-PBF	Laser beam powder bed fusion
LCF	Low cycle fatigue
304L SS	304L stainless steel
M/P	Machined and polished
SEM	Scanning electron microscope/microscopy
SR	Surface roughness
UTS	Ultimate tensile stress

studies intended to adopt different SR parameters such as R_t, R_v, R_{zISO}, etc. to better quantify the effect of SR on the fatigue behavior [14,26,31–38]. In summary, appropriate surface characteristic parameters capable of capturing the severity of the SR on the fatigue performance should be introduced before AM parts with AB surface conditions can be designed and considered for fatigue-critical applications.

In this study, the fatigue behavior of 304L stainless steel (304L SS) parts, manufactured via the laser beam powder bed fusion (LB-PBF) AM technique, with two different surface conditions, including AB and machined and polished (M/P) is investigated. SR measurements are conducted by a digital 3D microscope and values of various SR parameters are provided for a comprehensive understanding of the effects of surface texture on fatigue behavior. Both strain- and force-controlled fatigue tests are conducted and a previously established technique [24,39] to evaluate the fatigue performance for AM Ti-6Al-4V parts is utilized to predict the fatigue life of LB-PBF 304L SS specimens in AB surface conditions. The meta-stable nature of 304L SS (i.e. the tendency towards to martensite transformation) and its complex deformation behavior make it an excellent material to test concepts of fatigue resistance and failure mechanisms, particularly compared against a less complex, mostly elastic behavior such as the one for AM Ti-6Al-4V under cyclic fatigue loading. As such, the differences between strain-life and stress-life fatigue behaviors are also considered.

2. Experimental procedures

In this study, two different specimen types were fabricated vertically using an EOS M290 LB-PBF machine. Both net shape and oversized rectangular specimen blanks were fabricated to generate AB and M/P surface conditions. The round AB and M/P specimens with a straight gage section were designed to conform to ASTM E606 as shown in Fig. 1 [40] with the M/P specimens fabricated as rectangular blanks and machined to the final dimensions to minimize SR effects. The gage sections of the M/P specimens were manually polished using a series of abrasive silicon carbide papers to remove any machining marks which can cause early life crack initiations.

The specimens were produced using EOS M290 default process parameters recommended by the manufacturer for 316L stainless steel (SS). The details of the fabrication process parameters are as followed: layer thickness of 20 μm, hatching distance of 90 μm, scan speed of 1083 mm/s, laser power of 195 W, and using a carbon fiber recoater. The fabrication process was conducted under an argon environment maintaining an oxygen level below the threshold value, 1000 ppm. The entire build layout is shown in Fig. 2. The recoater brings the powder from East to West and the inert gas is infused from North to South with the front of the machine facing south.

The parts on the first column from the left side are ghost specimens which received 0 W laser power increasing the interlayer time interval to reduce the chance of failure often caused during the recoating process. Since residual stresses are not significant for vertical specimens

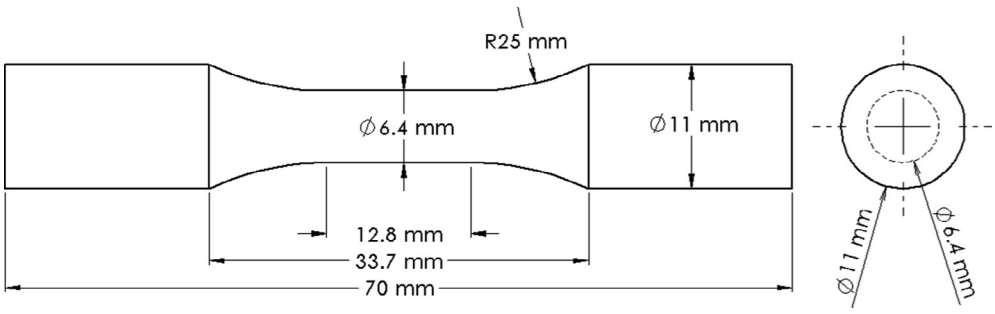

Fig. 1. Fatigue specimens designed based on ASTM E606, the standard test method for strain-controlled fatigue testing.

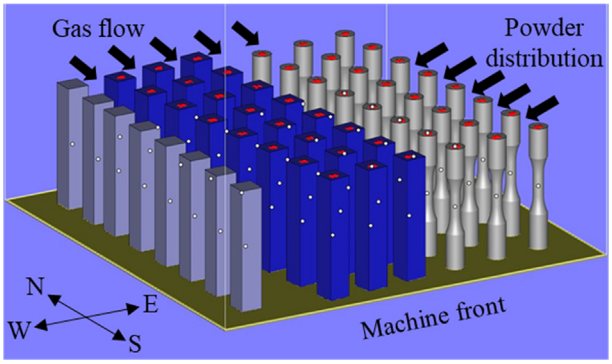

Fig. 2. The schematic build layout with cardinal points North, South, East, and West. Inert gas flows from North to South and the recoater distributes powder from East to West.

[41,42], no stress relief was conducted on the AB specimen or rectangular specimen blanks to avoid any environmental effects on the surface of the AB parts during heat treatment. The oversized rectangular specimen blanks in the middle were machined to the final shape of the round fatigue specimens with a straight gage section, given in Fig. 1. According to the ASTM E606 standard, the gage section of machined specimens was polished longitudinally after machining and the SR was reduced to ~0.2 μm [40]. The cylindrical parts on the right are the AB (net-shape) specimens, designed per Fig. 1. The 304L SS powder for this print was produced by LPW Technology Inc., with the reported particle size of 15–45 μm and the chemical composition as listed in Table 1.

The SR of the AB specimens was investigated parallel to the build and loading directions as shown in Fig. 3(a), using a Keyence VHX-6000 digital microscope. The microscope provides pixel-height data as CSV files that were analyzed using Matlab. For the present study, two-dimensional analysis along the scanned region, described as a yellow shaded area on the gage section, was conducted. Five lines were profiled on the scanned region as shown in Fig. 3(a) and investigated for every image to enhance statistical aspects of the surface roughness data. In order to consider the facing directional dependency, four cardinal directions were measured. Fig. 3(b) schematizes the four measured cardinal directions (North, East, South, and West) in relation to the gas inlet and the route of the recoater arm.

Strain- and force-controlled fatigue tests were conducted on both AB and M/P specimens. The uniaxial, fully reversed fatigue testing was conducted using an MTS landmark servohydraulic test frame with a load capacity of 100 kN. The strain and stress amplitudes were selected to cover both high cycle fatigue (HCF) and low cycle fatigue (LCF) regimes; strain amplitudes (ε_a) from 0.002 mm/mm up to 0.0075 mm/mm, stress amplitudes (σ_a) from 200 MPa up to 400 MPa, and frequencies from 0.5 Hz up to 5 Hz to maintain similar average cyclic strain/stress rates. The sinusoidal waveform was utilized for both force- and strain-controlled fatigue tests and an extensometer was mounted on the gage of the specimens for all strain-controlled fatigue tests. For HCF tests ($N > 10^6$ cycles), the test was paused at 1 million cycles and resumed with increased frequency after removal of the extensometer. If the reversals to failure reached 10^7, the tests were suspended and considered as run-out.

Failure for strain-controlled fatigue tests was considered as the life at which the stress dropped to approximately 70% of the maximum stress from recorded peak and valley data. On the other hand, the fatigue failure for force-controlled tests was considered when the specimens fractured. The final fracture surfaces after fatigue testing were investigated by a Zeiss Crossbeam 550 scanning electron microscope (SEM). The entire cross-sectional area was captured at ~20X to investigate the macroscopic fatigue crack characteristics. Higher magnification at ~100X was then used to observe the crack initiation sites at the surface. The area of the final catastrophic rupture was measured using ImageJ software.

3. Experimental results and discussion

3.1. Surface roughness

The values of different SR parameters, the arithmetical mean height of profiled line, R_a, the maximum peak-to-valley height of profiled line, R_t, and 10-point height roughness of profiled line, R_{zISO} were calculated using measured surface height data. The equations to calculate R_a, R_t, and R_{zISO} are expressed here [38]:

$$R_a = \frac{1}{l}\int_0^l |Z(x)|\, dx \quad (1)$$

$$R_t = |y_{max} - y_{min}| \quad (2)$$

$$R_{zISO} = \frac{1}{5}\left[\sum_{i=1}^{5} y_{i-max} + \sum_{j=1}^{5} y_{j-min}\right] \quad (3)$$

where l is the length of the measurement line, Z(x) is the height of point x along the measurement line, y_{max} is the maximum peak of the profile, and y_{min} is the minimum valley of the profile. For these surface parameters, five lines with a minimum length of 2 mm were used to get the mean and standard deviations and characterize the directional and locational dependencies of SR.

SR parameters for each facing direction (i.e. North, East, South, and West in Figs. 2 and 3) were investigated to decouple any directional effects on the fatigue behavior. The differences in surface texture are quantitatively shown in Table 2 and Fig. 4 with the directions corresponding to Fig. 3(a). Interestingly, the south facincg direction shows less variation in the measured data, which may be related to the lower extreme surface roughness values for each parameter when compared to the other directions. Despite these lower extreme values, however, the box and whisker chart provided in Fig. 4 suggests that none of the measured directional surface roughness parameters are significantly different. Such a lack of directional dependency on SR may be influenced by both a vertical build orientation and a cylindrical shape which reduce stair effects and friction of recoater. In addition, SR was measured from cylindrical specimens which provided geometrical disparity, hence it contains more variations. Although the directional dependency of SR was not significant in this study, it should be noted that more systematic studies, which are beyond the scope of this work, have reported some directional dependencies of LB-PBF Ti-6Al-4V [43].

The roughness related to the proximity to the inert gas inlet was also investigated to examine any locational dependence. The SR values of each specimen are listed in Table 3 including averages and standard deviations. Part locations on the substrate are schematically described in Fig. 5(a), and (b) shows the box whicker chart for the SR parameters related to specimens located either Northeast close to inert gas inlet, East, or Southeast close to the inert gas outlet. It should be noted that only the location dependency in relation to the gas injecting direction (from North to South) has been investigated in this study for the AB dog-bone specimens on the right side of the build plate in Fig. 5(a). The box plots in Fig. 5(b) indicate that while there are no clear statistical differences in SR among the three locations investigated (i.e. Northeast, East, and Southeast), a decreasing trend in R_t and R_{zISO} is somewhat noticeable with parts located further from the gas inlet having the lowest measured SR.

Table 1
The chemical composition of 304L SS powder, provided by LPW Technology.

C	Mn	P	S	Si	Cr	Ni	Fe
0.017	1.20	0.012	0.005	0.55	18.40	9.40	Bal

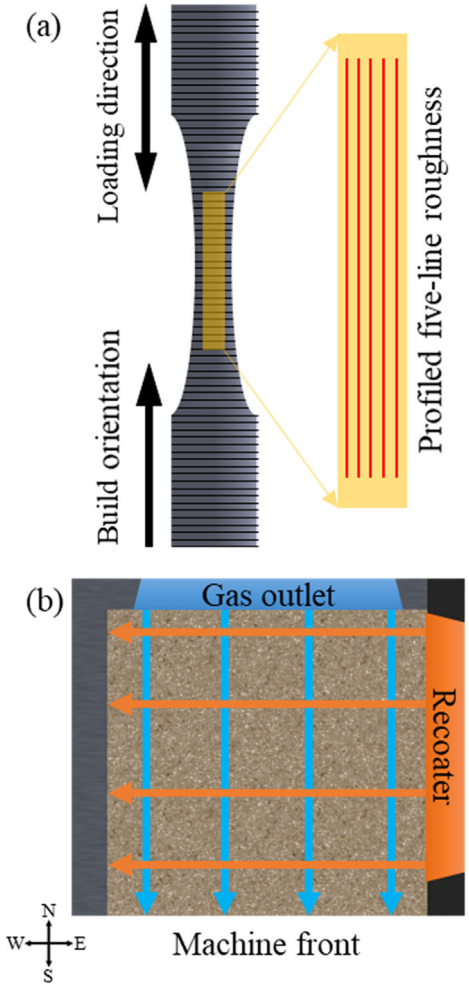

Fig. 3. The schematic describing: (a) the details of build orientation, load direction, and the profiled gage section on the specimen, and (b) the details of the four regions in relation to the EOS M290 build plate.

Table 2
Mean and standard deviation values of SR parameters, R_a, R_t, and R_{zISO} with AB surface condition for each facing direction. The unit is μm.

Facing directions	R_a	R_z	R_{zISO}
North	13 (2)	80 (14)	65 (11)
East	13 (2)	81 (13)	66 (10)
South	12 (1)	75 (7)	60 (4)
West	12 (3)	80 (15)	62 (12)

3.2. Fatigue behavior

The plastic and elastic strain amplitudes ($\frac{\Delta\varepsilon_p}{2}$ and $\frac{\Delta\varepsilon_e}{2}$), stress amplitude ($\sigma_a$), and mean stresses ($\sigma_m$) of strain-controlled tests were measured from the data recorded by the extensometer. For ε_a = 0.0075 mm/mm and ε_a = 0.003 mm/mm, mid-life hysteresis loops were always used as representative values, while the hysteresis loop at 10^6 cycles was used for M/P specimens at ε_a = 0.002 mm/mm, which exceeded 10^6 cycles. If the reversals to failure reached 10^7, the tests were suspended and considered as run-out. Strain-life and stress-life plots from strain- and force-controlled fatigue tests are presented in Fig. 6(a) and (b), respectively. The red data points represent the AB surface condition and the blue data points represent the M/P surface condition and arrows indicating run-out tests in both Fig. 6(a) and (b). The test of specimen fC_MP_10 was suspended due to grip failure as shown in Fig. 6(b).

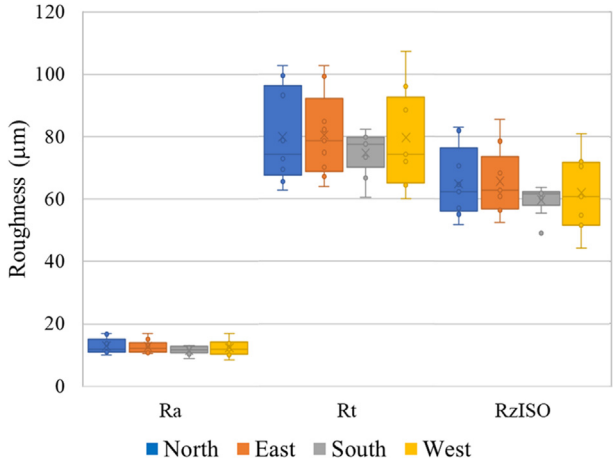

Fig. 4. Box and whisker plot of the various SR parameters and corresponding cardinal directions whithin the machine.

Table 3
Mean and standard deviation values of SR parameters, R_a, R_t, and R_{zISO} with AB surface condition for different locations on the substrate. The unit is μm.

Location of parts	R_a	R_z	R_{zISO}
Northeast	13 (2)	84 (11)	67 (8)
East	13 (3)	81 (16)	65 (13)
Southeast	11 (1)	71 (6)	57 (4)

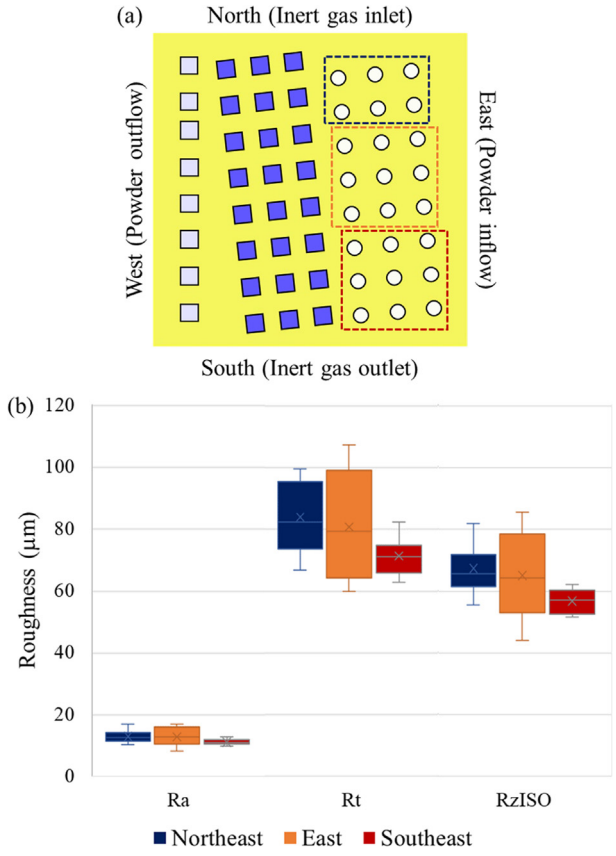

Fig. 5. (a) Schematically described build plate from the top view. Circles are AB dog-bone specimens and they are located restrictedly on the right side of the substrate. (b) Values of SR parameters describing the locational dependency of SR. The bars and error bars indicate means and standard deviations.

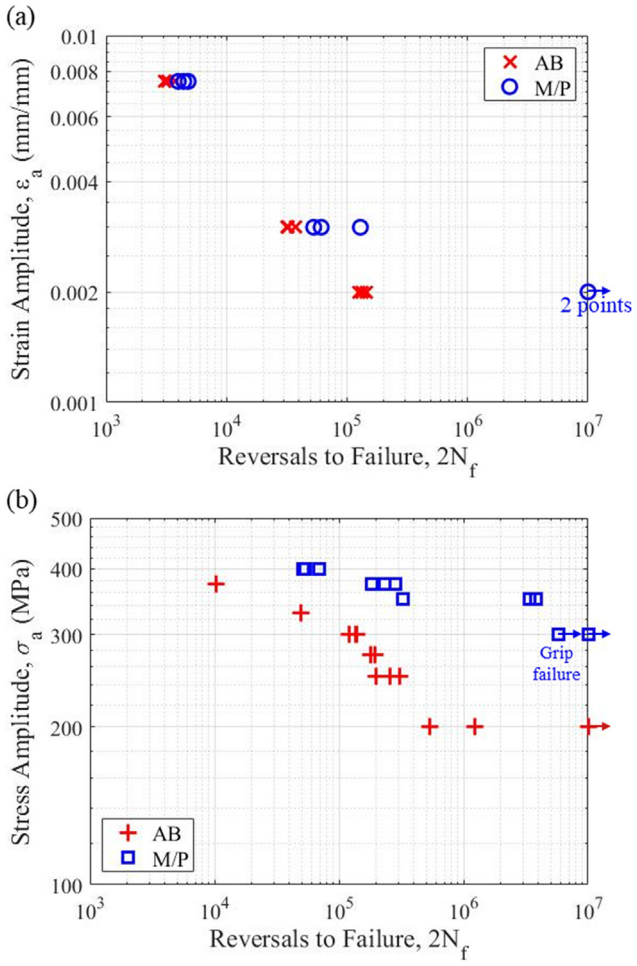

Fig. 6. (a) Strain-life and (b) stress-life plots from respectively strain-controlled and force-controlled fatigue tests of AB and M/P specimens.

The results presented in Fig. 6 show the detrimental effect of SR on fatigue strength exists under both strain- and force-control modes, however, the sensitivity to SR appears much greater for force-controlled tests (i.e. stress-life approach). As it can be seen in Fig. 6(a) for strain-life data, while no effect is seen in the LCF, significant effects of SR can be noticed in the HCF data. However, the significant effect of SR on the fatigue behavior is clearly visible in the stress-life data across all life regimens of LCF, intermediate cycle fatigue (ICF) and HCF.

Hysteresis loops for strain-controlled fatigue tests were generated by the strain data from the extensometer as shown in Fig. 7(a)–(d). The hysteresis loops in Fig. 7 represent the cyclic stress-strain behavior of the first and the ~mid-life cycle for both surface conditions at 0.0075 mm/mm and 0.003 mm/mm strain amplitudes. As seen, both AB and M/P specimens exhibit cyclic softening at both strain levels. The peak stress for the M/P specimens (Fig. 7(c) and (d)) are slightly higher than those measured for the AB specimens (Fig. 7(a) and (b)). This is because the true load-bearing cross-sectional area of AB specimens is smaller than the measured cross-sectional area including the SR using a caliper [14]. After considering R_t as a correction factor, the differences between peak stress of the M/P specimen and AB specimen was decreased from 6.7% to 1.6%. This result confirms that SR of AB specimen should not be included in the load-bearing region for stress calculations.

The cyclic stress-strain curves and data for specimens in AB and M/P surface conditions and the quasi-static tensile stress-strain curve are superimposed in Fig. 7(e). For AB specimens, revised load-bearing cross-sectional areas were used to calculate more precise stress values. The relationship between stress amplitude (σ_a) and measured plastic strain amplitude ($\frac{\Delta\varepsilon_p}{2}$) is provided by Eq. (4) [44]:

$$\sigma_a = K'\left(\frac{\Delta\varepsilon_p}{2}\right)^{n'} \tag{4}$$

where K' and n' are the cyclic strength coefficient and cyclic strain hardening exponent, respectively. K' and n' were calculated to be 591 MPa and 0.070 for AB specimens, and 587 MPa and 0.065 for M/P specimens, confirming that SR does not significantly influence the cyclic hardening/softening behavior. Accordingly, the cyclic stress-strain curves were generated by the Ramberg-Osgood relationship [45], expressed in Eq. (5), based on the obtained K' and n' for each set of specimens (i.e. AB and M/P):

$$\varepsilon_a = \frac{\Delta\varepsilon}{2} = \frac{\Delta\varepsilon_e}{2} + \frac{\Delta\varepsilon_p}{2} = \frac{\Delta\sigma}{2E} + \left(\frac{\Delta\sigma}{2K'}\right)^{1/n'} = \frac{\sigma_a}{E} + \left(\frac{\sigma_a}{K'}\right)^{1/n'} \tag{5}$$

The stress-strain plots in Fig. 7 demonstrate the considerable cyclic softening of LB-PBF 304LSS for both surface conditions. The complex cyclic deformation behavior of the LB-PBF 304L SS is shown for both strain- and force-controlled conditions in Fig. 8. The stress response for strain-controlled fatigue tests is shown for (a) ε_a = 0.0075 mm/mm, (b) ε_a = 0.003 mm/mm for both AB and M/P surface conditions, while the hysteresis loops for force-controlled tests at 375 MPa are provided for specimens in (c) AB and (d) M/P surface conditions. The plots in Fig. 8(a) and (b) illustrate cyclic softening for both AB and M/P specimens, and slightly greater maximum stress responses for M/P specimens. As discussed in preceding paragraphs, this different maximum stress response was caused by SR of AB specimens; hence, it can be neglected in calculations. Therefore, the stress-strain behavior of LB-PBF 304L SS over time are similar for these specimens regardless of their surface condition.

Secondary cyclic hardening was evident after approximately mid-life cycles for the ε_a = 0.0075 mm/mm tests according to Fig. 8(a). This secondary cyclic hardening behavior has also been observed in wrought 304L SS and is related to deformation induced martensitic transformation (DIMT) in this material [46–48]. The M/P stress response plot under high strain amplitude (ε_a = 0.0075 mm/mm) in Fig. 8(a) clearly shows substantial secondary hardening, while the AB specimen exhibits much less secondary hardening under the same strain amplitude. The M/P specimen starts cyclic hardening from ~650 cycles and progresses up to ~2000 cycles. The AB specimen also starts cyclic hardening from ~650 cycles, but failure occurs sooner than the M/P specimens, suggesting that lower fractions of DIMT are formed resulting in the lower observed secondary hardening. The reasons for this abrupt failure are discussed in detail in the following Fractography Analysis section.

Under the force-controlled condition, Fig. 8(c) and (d) show the deformation behavior is significantly different between the two surface conditions. In Fig. 8(c) and (d), black lines indicate early cycle (10th cycle) and red lines represent the last recorded cycle (5000th cycle for AB and 10^6th cycle for M/P surface condition) since the extensometer only recorded log data points. While in the early fatigue life the hysteresis loops are similar in size, the AB surface condition shows progressively greater plastic deformation in the later fatigue life stage. In addition to the increasing amount of plastic deformation, the specimen with AB surface condition also shows greater ratcheting (cyclic creep) compared to the one with M/P surface condition as indicated by the increasing mean strain in the final fatigue cycles. The remarkable expansion of the cyclic hysteresis loop and increasing mean strain suggests that the crack stability of specimens in AB surface condition deteriorates suddenly as compared to the specimens with M/P surface condition which will be discussed in detail in the fractography section.

The total strain-life curves of LB-PBF 304L SS based on strain amplitude and reversals to failure for AB and M/P specimens were generated by adding the elastic and plastic strain-life relations, expressed in Eq. (6):

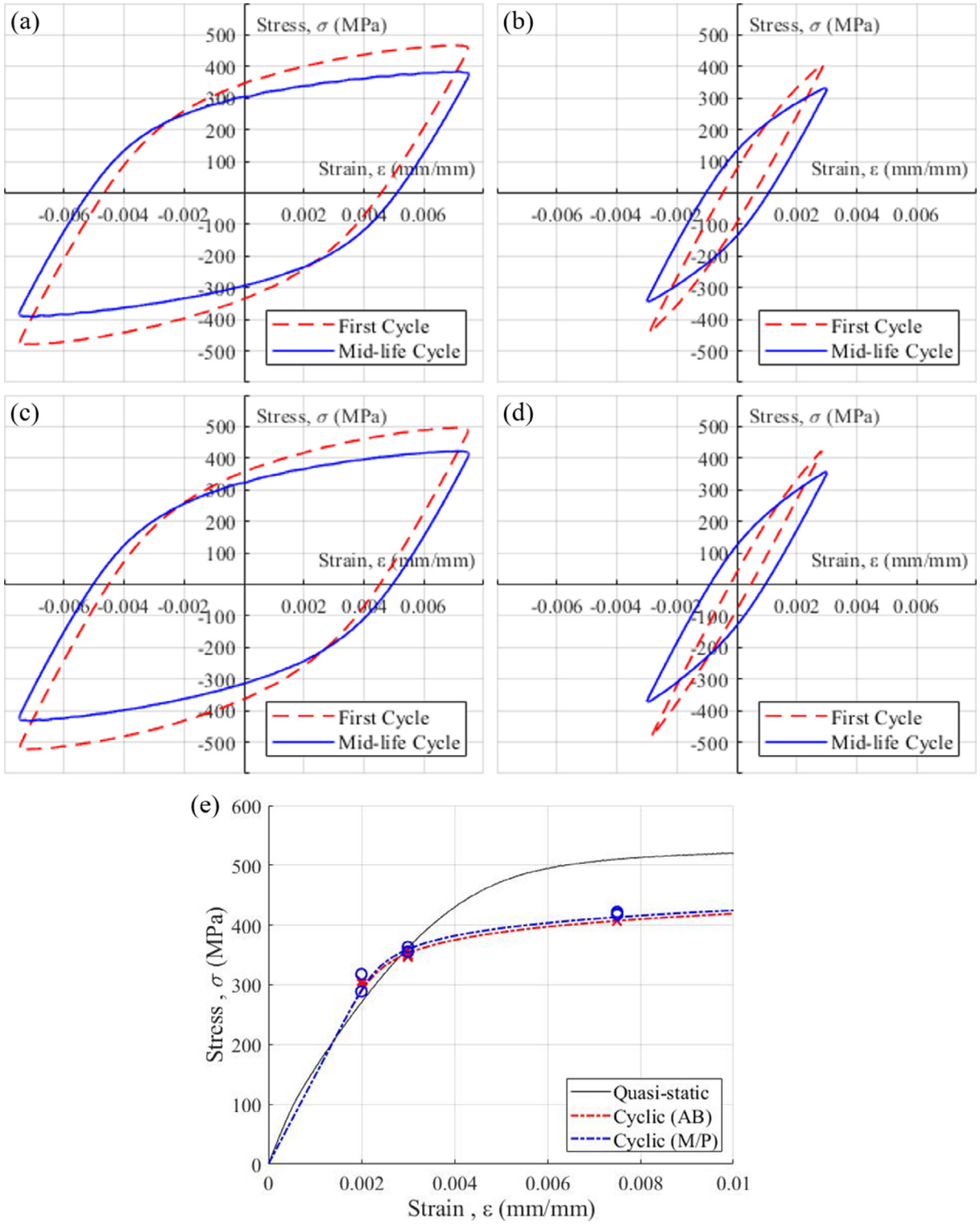

Fig. 7. Hysteresis loops of first and mid-life cycles for strain-controlled fatigue tests: (a) AB, $\varepsilon_a =$ 0.0075 mm/mm, (b) AB, $\varepsilon_a =$ 0.003 mm/mm, (c) M/P, $\varepsilon_a =$ 0.0075 mm/mm, and (d) M/P, $\varepsilon_a =$ 0.003 mm/mm. (e) Quasi-static tensile and cyclic stress-strain curves based on Ramberg-Osgood relationship.

$$\frac{\Delta\varepsilon}{2} = \varepsilon_a = \frac{\Delta\varepsilon_e}{2} + \frac{\Delta\varepsilon_p}{2} = \frac{\sigma_f'}{E}(2N_f)^b + \varepsilon_f'(2N_f)^c \quad (6)$$

where σ_f' and b are fatigue strength coefficient and exponent, and ε_f' and c are fatigue ductility coefficient and exponent [49]. All constants (σ_f', b, ε_f', and c) were calculated using practically measured plastic and elastic strain amplitudes as discussed previously. Each elastic and plastic strain fitted line was calculated from elastic and plastic strain amplitude data points, respectively, and added together to generate the total strain curve. Solid lines in Fig. 9(a) describe total strain-life curves for AB and M/P strain-controlled fatigue data. In addition, the dashed line and dash-dot line represent the elastic and plastic strain-life fitted curves, respectively. Obtained fatigue strength and ductility coefficients and exponents with 95% confidence bounds are listed in Table 4.

Comparing the AB and M/P fatigue curves in Fig. 9(a), some interesting observations can be made. For low-cycle strain-controlled

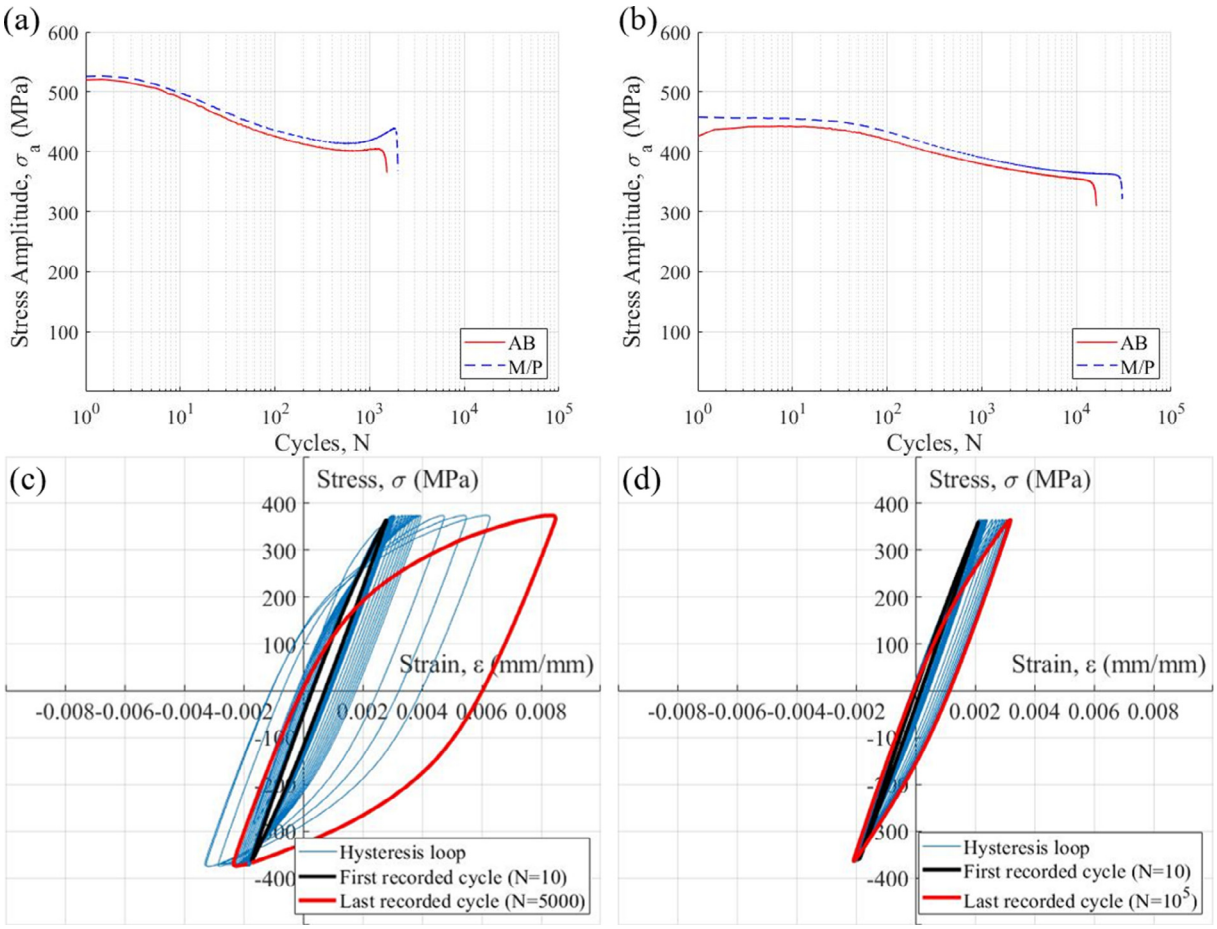

Fig. 8. Stress responses of strain-controlled fatigue tests for (a) ε_a = 0.0075 mm/mm and (b) ε_a = 0.003 mm/mm, as well as hysteresis loops of force-controlled tests for (c) σ_a = 375 MPa with AB surface condition and (d) σ_a = 375 MPa with M/P surface condition.

fatigue loading, the discrepancy in fatigue resistance between AB and M/P specimens is minimal. In general, the fatigue life in the LCF regime is dominated by crack growth as the high amount of plasticity results in cracks initiating in the early stage of fatigue life. As such, the effect of SR on crack initiation is less prominent and the crack growth behavior, which is more influenced by the microstructure, has a greater effect on the LCF strength. As the strain amplitude decreases, the effect of SR becomes increasingly detrimental as observed at ε_a = 0.002 mm/mm, where the fatigue life of the AB specimens is at least an order of magnitude lower than the ones for the M/P specimens. In the HCF regime, the fatigue life is dominated by crack initiation such that surface features associated with AB SR are much more detrimental to the fatigue strength.

For force-controlled fatigue testing results (stress-life data), the Basquin's stress-life curves of LB-PBF 304L SS specimen in both surface conditions are shown in Fig. 9(b). The details regarding Basquin's equation are provided in Eq. (7):

$$\sigma_a = \sigma_f'(2N_f)^b \quad (7)$$

where σ_a is the applied alternating stress, σ_f' is the fatigue strength coefficient and represents the value of σ_a at the first cycle, and b is the fatigue strength exponent or slope of the log-log stress-life curve [49]. The calculated coefficients and exponents for both surface conditions are listed in Table 4 with 95% confidence bounds.

Based on the above investigations for each control mode, the surface condition seems to have minimal effect on the fatigue strength in the LCF and ICF regime of the strain-controlled fatigue tests. As shown in Fig. 9(a), differences between AB and M/P are 220 reversals at ε_a = 0.0075 mm/mm (eC_AB_3 versus eC_MP_1) and 15,592 reversals at ε_a = 0.003 mm/mm (eC_AB_6 versus eC_MP_4). In the HCF regime, the surface condition affected the strain-life fatigue behavior of the LB-PBF 304L SS specimens considerably. For example, at ε_a = 0.002 mm/mm, more than 2 orders of magnitude difference in reversals to failure between AB and M/P specimens can be noticed in Fig. 9(a) (eC_AB_7 versus eC_MP_7).

Under the force-controlled testing, M/P specimens always exhibited better fatigue performance than the AB specimens regardless of the life regime, as evident from the stress-life plot in Fig. 9(b). For example, at σ_a = 375 MPa which can be considered as the ICF regime, more than an order of magnitude difference in reversals to failure between AB and M/P specimens can be seen in Fig. 9(b). Lower stress amplitudes resulted in a larger disparity between AB and M/P test specimens with the AB condition showing almost two orders of magnitude decrease in fatigue strength at σ_a = 300 MPa compared to the M/P condition (fC_AB_3 versus fC_MP_11).

In general, the stress-life behavior showed a greater sensitivity to SR compared to the strain-life behavior. This discrepancy in loading effects is believed to be related to the remarkable damage tolerance of 304L SS such that the fatigue life is dominated by the deformation behavior of the material. Under force-controlled loading, the crack stability deteriorates resulting in abrupt tensile fracture of the specimen, whereas under strain-controlled loading the deformation is controlled, allowing the crack to maintain stability through the entirety of the gage section. Table 5 demonstrates this behavior by comparing the accumulated plastic strains throughout the life of some specimens with different surface conditions and tested under different control modes. Accumulated plastic strains were calculated as the sum of the measured plastic strains from the hysteresis loops. Since only logarithmic cycles were

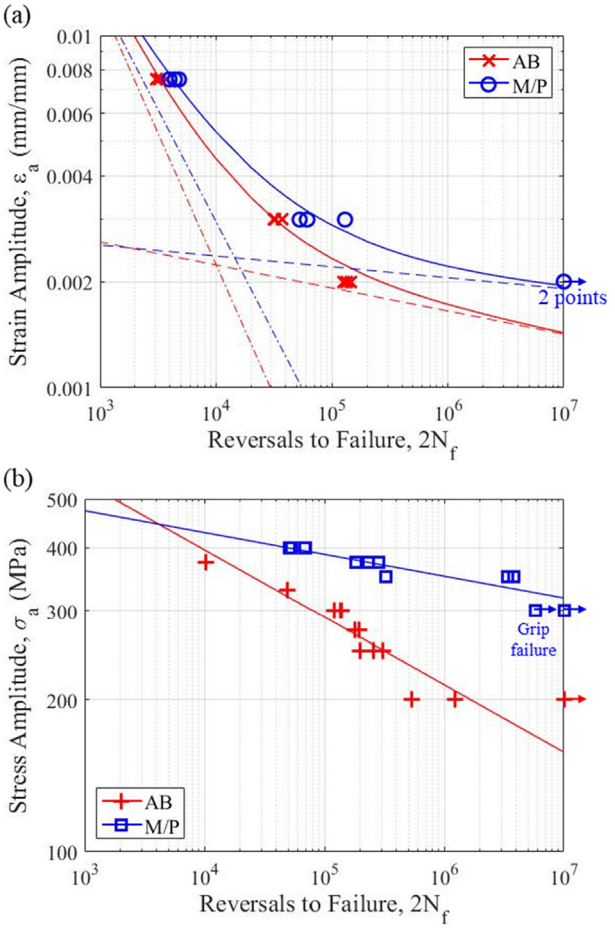

Fig. 9. (a) Strain-life curves and fatigue data, as well as, (b) Basquin's stress-life curves and fatigue data for specimens in AB and M/P surface conditions. The dashed line and dash-dot line in (a) represent the elastic and plastic strain-life fitted curves, respectively.

Table 4
Strain-life and stress-life fatigue properties for LB-PBF 304L SS with AB and M/P surface conditions. The 95% confidence bounds are also provided.

		Surface conditions	
		AB	M/P
Strain-Life	σ_f'(MPa)	471 (418, 524)	364 (281, 446)
	B	−0.07 (−0.08, −0.05)	−0.03 (−0.05, −0.01)
	ε_f'(mm/mm)	2.1180(−0.3026, 4.5380)	1.0310(−0.7099, 2.7730)
	C	−0.74(−0.88, −0.60)	−0.64(−0.83, −0.44)
Stress-Life	σ_f'(MPa)	1359(847, 1871)	639(497, 782)
	B	−0.13(−0.17, −0.10)	−0.04(−0.06, −0.03)

recorded, the plastic strains of the intermediate cycles were taken from the most recent measured cycle.

The accumulated plastic strain for M/P specimens is higher than the AB specimens for both control modes. The difference in accumulated plastic strain between surface conditions for strain-controlled mode is only 11.62 mm/mm, however, the difference for force-controlled mode is 46.17 mm/mm. Additionally, while the force-controlled M/P has almost twice the accumulated plastic strain as that of the M/P strain-controlled test, the force-controlled AB specimen has approximately half of the accumulated plastic strain as compared to the one for the AB strain-controlled specimen. The larger plastic strain accumulation for the M/P force-controlled condition can be explained by the increasing deformation resulting from the increasing true stress when accounting for the decreasing load bearing area during the crack propagation in the specimen. However, during the strain-controlled test, such an increase in stress is not expected because of the reduction in the force response as the stiffness drops as the crack propogates through the specimen. The unstable deformation behavior for the force-controlled AB specimens shown in Fig. 8(c) leads to early fatigue failure resulting in the lowest measured accumulated plastic strain and accounting for the large disparity between AB and M/P surface conditions. This disparity in accumulated plastic strain between the surface conditions under force-controlled mode suggests an abrupt disruption to the crack stability may be responsible for the greater sensitivity to SR.

3.3. Fractography analysis

The events leading to final fracture are distinct, and therefore, provide information regarding crack initiation and propagation mechanisms. Fig. 10 shows the final fracture surfaces under ε_a = 0.003 mm/mm with (a) AB and (b) M/P surface conditions. The entire fracture surfaces, as well as the magnified crack initiation sites, are presented in these images. In Fig. 10(a), arrows, dashed lines, and shaded areas with red color indicate crack initiations, the early stage of crack propagations, and surface defects, respectively. The multiple initiated cracks in AB specimen, shown in Fig. 10(a), grew, coalesced, and grew further until the final fracture. In contrast, the cracks of M/P specimens shown in Fig. 10(b) were not solely initiated on the surface, but also by internal defects close to the surface. Lack-of-fusion defects highlighted as shaded areas were observed in both surface region and internal part of M/P specimens, as shown in enlarged images of Fig. 10(b). While the surface crack dominates the crack growth, it coalesces with multiple internal cracks but maintains stability and propagates through the entirety of the specimen under strain-controlled testing, as seen in Fig. 10(b).

Fracture surfaces for force-controlled specimens were strikingly different than the strain-controlled specimens. Fig. 11(a) and (b) show the fracture surfaces of AB and M/P specimens both tested at σ_a = 375 MPa. The cracks in AB specimens under force-controlled loading similarly started on the surface at multiple locations as described in Fig. 11(a), however, the shear lips visible at the merging point of these cracks suggest that the failure occurred abruptly once the cracks coalesced. For the M/P specimens, there were relatively fewer crack initiations sites at the surface; however, there were multiple cracks generated from the internal lack-of fusion defects, as shown in enlarged images in Fig. 11(b). The internal cracks of M/P specimens did not develop as rapidly as the surface cracks associated with the AB condition, which is related to the lower driving force of internal cracks compared to surface cracks. The smaller internal cracks coalesced with the dominant crack initiated from the surface and maintained stable

Table 5
Examples of accumulated plastic strain throughout the life of select specimens from strain- and force-controlled fatigue tests with AB and M/P surface conditions.

Control mode	Surface condition	Specimen ID	ε_a or σ_a (mm/mm or MPa)	$\varepsilon_{p,acc}$(mm/mm)	$2N_f$ (reversals)
Strain control	AB	eC_AB_5	0.003	16.70	32,448
	M/P	eC_MP_5	0.003	28.32	60,986
Force control	AB	fC_AB_1	375	8.44	10,370
	M/P	fC_MP_5	375	54.61	231,782

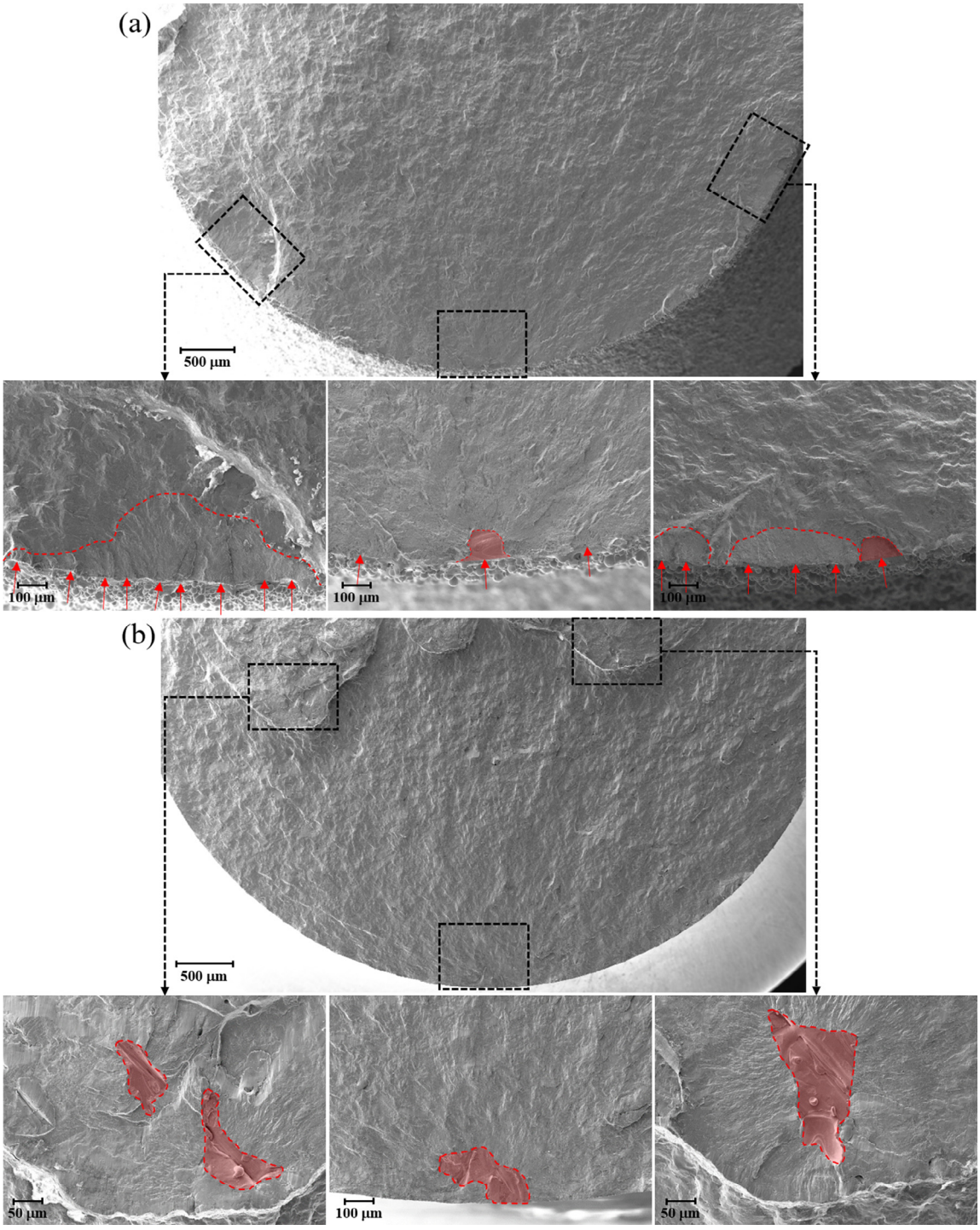

Fig. 10. Observed final fracture surfaces for strain-controlled fatigue test under ε_a = 0.003 mm/mm for specimens with (a) AB and (b) M/P surface conditions. Arrows, dashed lines, and shaded areas with a red color in (a) show crack initiations, the early stage of crack propagations, and defects at the surface, respectively. The shaded areas in (b) describe defects caused by lack-of-fusions.

crack growth, i.e. did not fail abruptly at the point of a merger as was the case for the AB specimens.

Comparing the AB and M/P fracture characteristics suggest that the greater sensitivity to SR of force-controlled tests can be correlated to the sudden loss of crack stability for the AB condition when multiple cracks coalesce. The area of crack propagation was measured for these two surface conditions in Fig. 11 for force-controlled tests and show that the stable crack growth region of the AB surface condition is approximately 29%, while it is approximately 45% for the M/P condition. This in conjunction with the unstable deformation behavior shown in the AB hysteresis loops presented in Fig. 8(c) demonstrates the sudden loss of stability for the AB surface condition can be attributed to the fast propagation of cracks initiated from the surface and them quickly merging with each other.

Under stress-based conditions (i.e. force-controlled testing), the true stress increases significantly as the cracks grow and the coalesce from multiple cracks and promotes crack instability, ultimately yielding shorter fatigue lives. Under strain-based loadings (i.e. strain-controlled testing), the deformation is controlled, so despite the decreasing load bearing area attributed to crack growth, stiffness drops, the stress

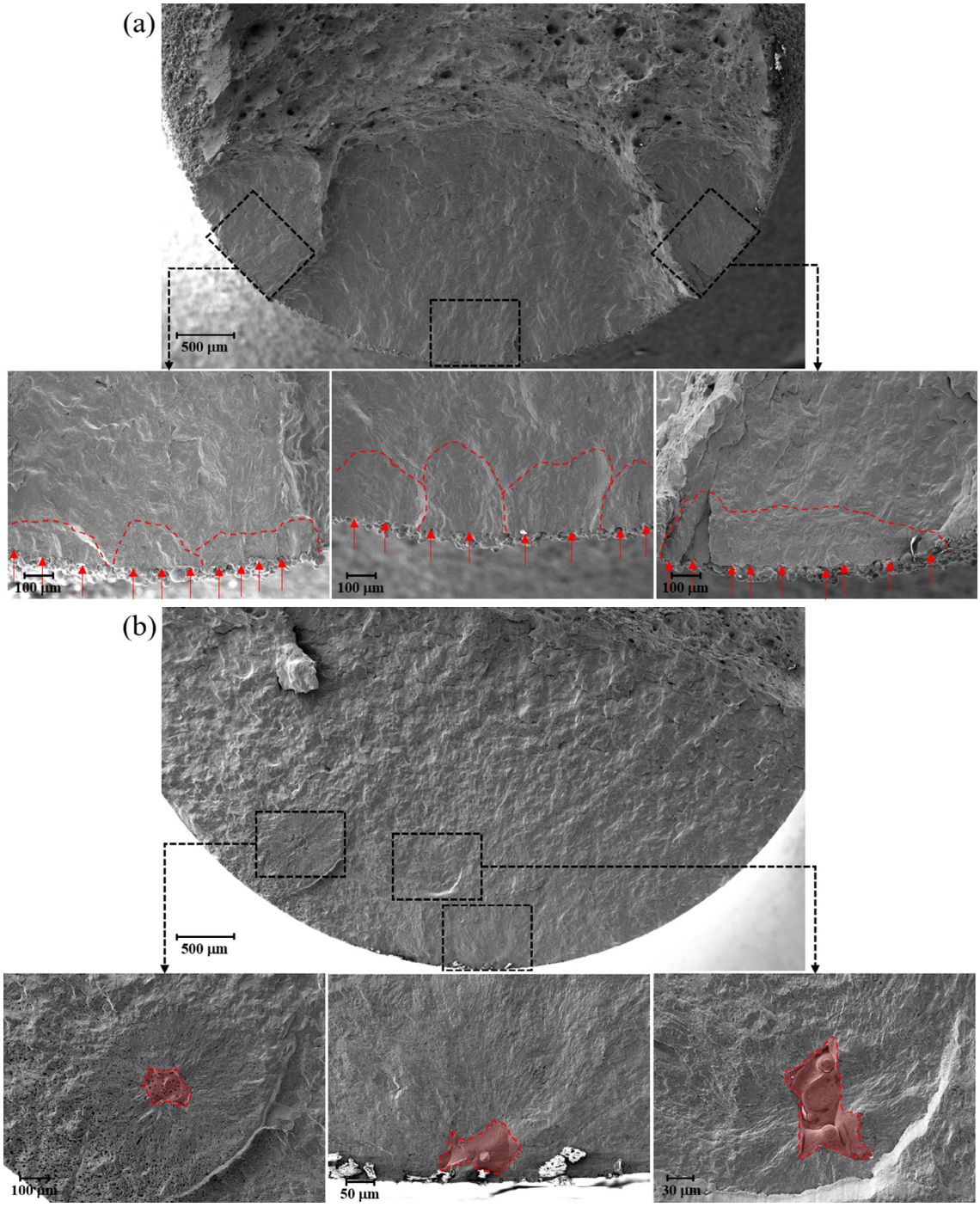

Fig. 11. Observed final fracture surfaces for force-controlled fatigue test under σ_a = 375 MPa for specimens with (a) AB and (b) M/P surface conditions. Red arrows and dashed lines in (a) show crack initiations and early stage of crack propagations, respectively. The shaded areas in (b) describe defects caused by lack-of-fusions.

response does not increase as much, and crack stability is maintained throughout the fatigue life. As such, the strain-life fatigue behavior is less sensitive to SR as compared to stress-life fatigue behavior.

4. Fatigue life estimations based on surface roughness

The characterized fracture surfaces show that SR can be a dominant factor in crack initiation and the reason for the shorter fatigue lives in AB specimens. AB surface topology can be categorized by peaks and valleys with un-melted or partially melted powder particles mostly contributing to the peaks. The peaks on the surface do not affect the fatigue behavior, however, the valleys on the surface of AB specimens act as micro-notches promoting early life crack initiation [24]. As a result, the AB specimens can be considered as notched specimens due to SR, with the most severe notches contributing to the lower fatigue resistance of AB specimens. Several factors dictate the severity of micro-notch with the depth and sharpness of the valley most likely being the dominant characteristics.

In order to estimate the effect of SR on fatigue strength in this study, the SR is considered as micro-notches and the stress concentration factors are calculated based on the Arola-Ramulu model [39,50]. Height-pixel SR data generated by digital focal variation microscopy are evaluated. The maximum peak-to-valley roughness (R_t), 10-point height roughness (R_{zISO}), and 10-point valley radii ($\bar{\rho}_{10}$) were calculated

using Eqs. (2), (3), and (8), respectively:

$$\bar{\rho}_{10} = \frac{1}{5}\left[\sum_{j=1}^{5} \rho_{j-min}\right] \quad (8)$$

where ρ_j are the radii of the deepest valleys. To minimize the error of height-pixel analysis, the Gaussian filter was applied [51].

The notch sensitivity of the material (q), the effective elastic stress concentration factor ($\bar{K}_t$), and the effective fatigue notch factor ($\bar{K}_f$) need to be calculated using surface characteristics values; R_a, R_t, R_{zISO}, and $\bar{\rho}_{10}$. The relationships between these parameters are expressed in Eqs. (9), (10), and (11) [39,52]:

$$q = 1/\left(1 + \frac{\gamma}{\bar{\rho}_{10}}\right) \quad (9)$$

$$\bar{K}_t = 1 + n\left(\frac{R_a}{\bar{\rho}_{10}}\right)\left(\frac{R_t}{R_{zISO}}\right) \quad (10)$$

$$\bar{K}_f = 1 + q(\bar{K}_t - 1) \quad (11)$$

where the stress state (n) is assumed to be 2 for the tension and the material characteristic length(γ) is considered to be 13 μm based on the LB-PBF 304L SS average grain size [53]. Accordingly, the average and standard deviation of surface characteristics values (i.e. R_a, R_t, R_{zISO}, and $\bar{\rho}_{10}$) , the effective elastic stress concentration factors and the effective fatigue notch factors (i.e. q, $\bar{K}_t$, $\bar{K}_f$) for AB specimens are calculated and listed in Table 6. Since the values were generated by the data from many specimens with four directions (with a total of 180 profiled lines), the results can be considered statistically reliable.

The stress-life behavior of M/P specimens were estimated using ultimate tensile stress (UTS) of LB-PBF 304L SS [53], 650 MPa, and experimentally obtained fatigue endurance limit, 300 MPa at 10^7 reversals. The fatigue strength fraction factor, f = 0.85, was acquired by UTS [54] and the fatigue strength, 553 MPa at 2000 reversals, was calculated by using obtained f and UTS. The stress-life curve is generated as a straight line through the estimated fatigue strength at 2000 reversals and the experimental endurance limit at 10^7 reversals, which is described as a blue line in Fig. 12(a). To estimate the AB stress life curve, the experimentally obtained endurance limit of M/P specimens, 300 MPa was divided by the estimated effective fatigue notch factor, $\bar{K}_f$ = 2.30, calculated based on the SR and methodology explained above, to estimate the endurance limit of AB specimens. The calculated endurance limit of AB specimens, 130 MPa at 10^7 reversals, is connected as a red line with the estimated fatigue strength, 553 MPa at 2000 reversals as shown in Fig. 12(a).

As seen in Fig. 12(a), the estimated AB line generated by SR parameters, endurance limit of M/P specimens, UTS, and fatigue strength fraction, captures the detrimental effect of the SR on the stress-life fatigue behavior of AB specimens. Furthermore, the predicted versus the experimentally observed fatigue lives of AB specimens under force-controlled testing with a scatter band of two is given in Fig. 12(b). All data points fall within the scatter band of two demonstrating the effectiveness of predicting the stress-life behavior of AB specimens based on SR and the procedure described above. It is worth reminding that the stress-life curve for AB specimens is generated without the use of any AB fatigue data and it seems to provide an effective design tool when data related to a particular SR is not available.

The other approach to correct the stress-life fatigue behavior for the effect of SR is to use the power law equation; for example, Basquin or Tri-Slope approach. It is well established that the SR affects the slope of the stress-life curve in the HCF regime [49]. If the stress-life fatigue properties of M/P specimens are available, the stress-life curve for AB specimens can be potentially estimated based on the effective fatigue notch factor ($\bar{K}_f$) calculated for the relevant SR and the assumed run-out number of reversals. For example, the Basquin equation for M/P specimens can be revised to capture the effect of SR for parts that are not machined/polished or have undergone other techniques of surface treatments as follows:

$$\sigma_a = \sigma_f'(2N_f)^{b-0.143\log(\bar{K}_f)} \quad (12)$$

where σ_f' and b are the coefficient and exponent of the power-curve (either using Basquin or Tri-Slope methods) to the stress-life data of M/P specimens based on 10^7 number of reversals for the run-out tests. The effective fatigue notch factor ($\bar{K}_f$) can be calculated from Eqs. (2), (3), and (8)–(11). It is worth noting that the Tri-Slope method typically provides a better fit to stress-life data, and therefore, it is also recommended here to use the coefficient and exponent of the power-curve to the ICF/HCF stress-life data based on the Tri-Slope approach. Again it should be mentioned that no fatigue data for the material with SR is needed in Eq. (12) and the information about the SR will be adequate for the described fatigue life calculations.

Fatigue strength of LB-PBF 304L SS specimens in AB surface condition under strain-controlled loading was also estimated by the effective fatigue notch factor approach as shown in Fig. 13 using the same approach for calculating the effective fatigue notch factor $\bar{K}_f$ = 2.30 for AB specimens. There are not many effects of SR in LCF due to the significant presence of plastic deformation, while the effects of SR are primary in HCF where elastic strain is dominant. In order to adapt the influence of SR, the elastic portion of the total strain-life curve of M/P specimens is solely adjusted based on the calculated effective fatigue notch factor [49]. The elastic strain amplitude at 10^7 reversals, $\frac{\Delta\varepsilon_e}{2}$ = 0.0019 mm/mm, was obtained from the fitted elastic strain-life curve of M/P specimens, and then it was divided by $\bar{K}_f$ = 2.30 to estimate the effect of SR. The estimated elastic strain amplitude at 10^7 reversals, $\frac{\Delta\varepsilon_e}{2}$ = 0.0008 mm/mm, is connected as a red dashed line in Fig. 13(a) with elastic strain of M/P specimens at the first reversal, $\frac{\Delta\varepsilon_e}{2}$ = 0.0034 mm/mm. As a result, the estimated elastic strain-life curve of AB specimens was added to the plastic strain-life curve of M/P specimens, resulting in the total estimated strain-life curve of AB specimens as a solid red curve in Fig. 13(a).

Alternatively, the elastic portion of the total strain-life equation generated from the fitted curves to M/P strain-life fatigue data can be adjusted for the fatigue strength exponent based on the effective fatigue notch factor ($\bar{K}_f$) calculated from Eqs. (2), (3), and (8)–(11). Based on the 10^7 run-out reversals considered in this study the total strain-life equation for specimens with SR can be written as:

$$\frac{\Delta\varepsilon}{2} = \varepsilon_a = \frac{\Delta\varepsilon_e}{2} + \frac{\Delta\varepsilon_p}{2} = \frac{\sigma_f'}{E}(2N_f)^{b-0.143\log(\bar{K}_f)} + \varepsilon_f'(2N_f)^c \quad (13)$$

where σ_f', b, ε_f', and c are obtained from strain-life fatigue data of M/P specimens. The only information from the specimens with SR needed in this approach is the surface topography to calculate $\bar{K}_f$, as no AB fatigue data is utilized.

The estimated versus experimentally observed fatigue lives of AB specimens under strain-controlled loading with scatter bands of two is shown in Fig. 13(b). All estimated fatigue lives again fall within the scatter bands of two from experimentally obtained fatigue lives. Fatigue strength estimation using a effective fatigue notch factor based on SR parameters successfully predict fatigue lives of AB specimens not only under force-controlled (stress-life) but also under strain-controlled (strain-life) fatigue tests. However, it should be noted that the prediction method is distinct for each control mode. In terms of using the SR parameters and the experimentally obtained fatigue data for M/P specimens, these estimation approaches show great potential as non-

Table 6
Calculated SR characteristics, effective stress concentration factors, and effective fatigue notch factors for fatigue life estimation of AB specimens.

	R_a(μm)	R_t(μm)	R_{zISO}(μm)	$\bar{\rho}_{10}$(μm)	q	$\bar{K}_t$	$\bar{K}_f$
Average (STD)	12 (2)	79 (13)	63 (10)	12 (4)	0.45 (0.09)	4.12 (1.41)	2.30 (0.36)

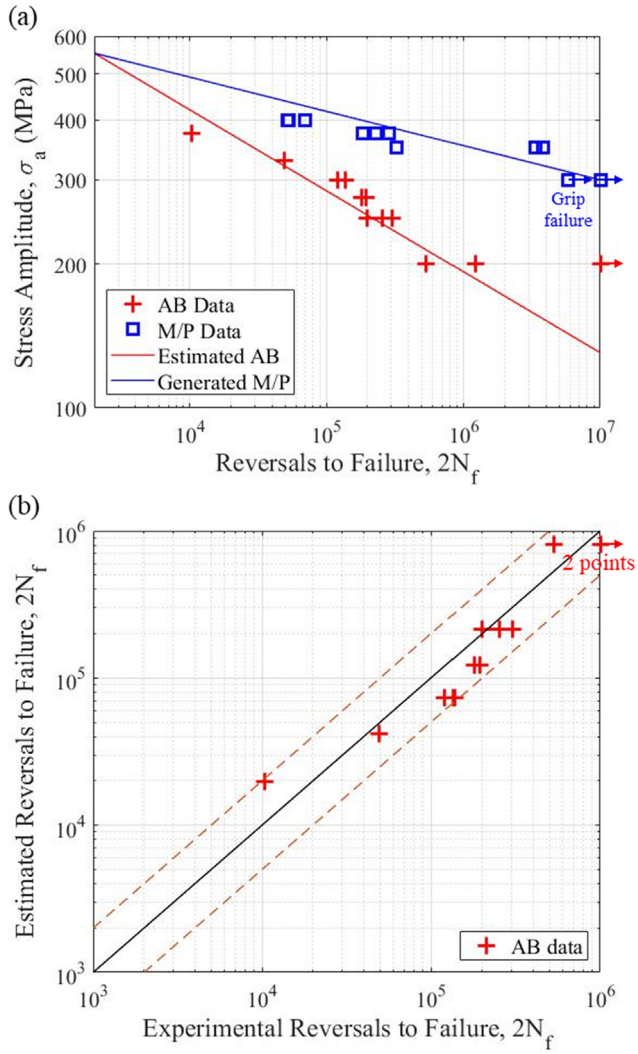

Fig. 12. (a) Stress-life fatigue plot with estimated fatigue strength using the endurance limit of M/P data, a fatigue strength fraction with UTS, and an effective fatigue notch factor based on SR parameters. (b) Estimated fatigue lives compared to experimentally obtained fatigue lives with the scatter bands of two for AB specimens.

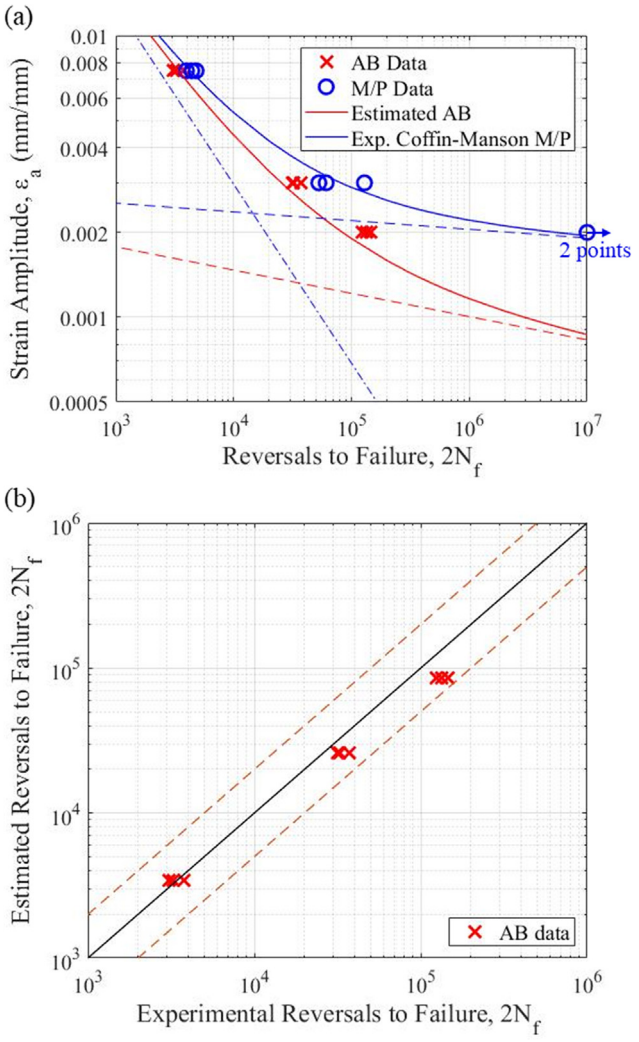

Fig. 13. (a) Strain-life fatigue plot based on experimental data for M/P specimens and estimated curve for AB specimens based on correcting the elastic strain behavior using an effective fatigue notch factor with SR parameters. The blue dashed line and dash-dot line represent the experimentally obtained elastic and plastic strain-life of M/P specimens. The red dashed line represents the estimated elastic strain-life of AB specimens. (b) Estimated fatigue lives compared to experimentally obtained fatigue lives with the scatter bands of two.

destructive fatigue life prediction methods for parts with SR typical to AM processes.

5. Conclusions and future outlook

The main objective of this research was to assess the effect of surface roughness and loading (i.e. force versus deformation) on the cyclic deformation and fatigue behavior of LB-PBF 304L SS. Through a rigorous experimental approach, the sensitivity to surface roughness was investigated for both stress-based and strain-based fatigue testing through post-mortem fracture analysis, and classical fatigue modeling approaches. Several interesting and impactful conclusions can be drawn from this study as listed here:

1. Surface roughness measurements on the various faces and specimens from different locations on the build plate suggest that while directional effects on surface roughness are minimal, there is a certain locational dependency based on the position of the part relative to the inert gas inlet. However, the effect of locational dependency on the surface roughness of LB-PBF 304L SS was also found to not be statistically significant.
2. The crack initiation for the as-built specimens is dominated by the surface features in the high cycle fatigue regime resulting in an early fatigue life crack initiation, while defects at or near the surface are the dominant initiation mechanisms for the specimens with machined/polished surfaces.
3. The low cycle fatigue regime shows little to no effect from surface roughness for strain-based fatigue loading, indicating the microstructure is more influential to the fatigue life despite the presence of surface roughness (i.e. potential stress concentrations) at the surface of as-built specimens.
4. The sensitivity to surface roughness is thus dependent on the loading condition with strain-based fatigue loadings showing lower sensitivity to roughness, particularly in the low cycle fatigue regime. Under stress-based fatigue loading, the sensitivity to surface roughness was observed for all stress levels and increased significantly for the lower stress amplitudes.
5. The general effect of surface roughness on the stress-life fatigue behavior of LB-PBF 304L SS can be adequately estimated using standard surface roughness parameters, a geometrical parameter based on notch sharpness, ultimate tensile strength, grain size, and

smooth surface endurance limit. Fatigue life predictions for specimens with as-built surface roughness utilizing this approach fall within scatter bands of two from experimentally obtained fatigue lives.

6. For strain-based fatigue loading, a classical approach utilizing a surface factor to correct the elastic portion of the total strain-life curve can adequately capture the surface roughness effects. Fatigue life predictions utilizing this approach also fall within scatter bands of two from experimentally obtained fatigue lives for specimens in as-built surface condition.

In closing, the results and analysis presented in this study demonstrate a simple approach for predicting the detrimental effect of as-built surfaces on the fatigue behavior for both stress- and strain-based loads. While these results have shown success for both 304L SS and Ti-6Al-4V [24], which show vastly different cyclic stress-strain behaviors, additional studies on other additive manufactured metals including post processing are necessary to further validate this method. For example, Ni-based superalloys are particularly interesting as AM is increasingly being explored for fabricating high temperature turbine blades with internal cooling channels. Additionally, as Ni-based superalloys and many other materials require extensive post-process including surface and thermal treatments to achieve desired mechanical performance, understanding the influence of such treatments on the surface condition and resulting fatigue resistance is critical. Showing success of this approach for additional material systems and surface conditions would further advance additive manufacturing as a universally applicable technology to fabricate fatigue and fracture critical components with complex geometries.

Declaration of Competing Interest

The authors declare that they have no known competing financial interests or personal relationships that could have appeared to influence the work reported in this paper.

Acknowledgments

This material is based upon work partially supported by the National Institute of Standards and Technology (NIST) under Award Nos. 70NANB18H220 and 70NANB19H170. Sandia National Laboratories is a multimission laboratory managed and operated by National Technology and Engineering Solutions of Sandia LLC, a wholly owned subsidiary of Honeywell International Inc. for the U.S. Department of Energy's National Nuclear Security Administration under contract DE-NA0003525. This paper describes objective technical results and analysis. Any subjective views or opinions that might be expressed in the paper do not necessarily represent the views of the U.S. Department of Energy or the United States Government.

Appendix A. Supplementary material

Supplementary data to this article can be found online at https://doi.org/10.1016/j.ijfatigue.2020.105856.

References

[1] DebRoy T, Wei HL, Zuback JS, Mukherjee T, Elmer JW, Milewski JO, et al. Additive manufacturing of metallic components – process, structure and properties. Prog Mater Sci 2018;92:112–224. https://doi.org/10.1016/j.pmatsci.2017.10.001.
[2] Frazier WE. Metal additive manufacturing: a review. J Mater Eng Perform 2014;23:1917–28. https://doi.org/10.1007/s11665-014-0958-z.
[3] Vayre B, Vignat F, Villeneuve F. Metallic additive manufacturing: state-of-the-art review and prospects. Mech Ind 2012;13:89–96. https://doi.org/10.1051/meca/2012003.
[4] Herzog D, Seyda V, Wycisk E, Emmelmann C. Additive manufacturing of metals. Acta Mater 2016;117:371–92. https://doi.org/10.1016/j.actamat.2016.07.019.
[5] Guo N, Leu MC. Additive manufacturing: Technology, applications and research needs. Front Mech Eng 2013;8:215–43. https://doi.org/10.1007/s11465-013-0248-8.
[6] Gu DD, Meiners W, Wissenbach K, Poprawe R. Laser additive manufacturing of metallic components: materials, processes and mechanisms. Int Mater Rev 2012;57:133–64. https://doi.org/10.1179/1743280411Y.0000000014.
[7] Gong X, Anderson T, Chou K. Review on powder-based electron beam additive manufacturing technology. Manuf Rev 2014;1:2. https://doi.org/10.1051/mfreview/2014001.
[8] Shamsaei N, Yadollahi A, Bian L, Thompson SM. An overview of Direct Laser Deposition for additive manufacturing; Part II: Mechanical behavior, process parameter optimization and control. Addit Manuf 2015;8:12–35. https://doi.org/10.1016/j.addma.2015.07.002.
[9] Yadollahi A, Shamsaei N. Additive manufacturing of fatigue resistant materials: challenges and opportunities. Int J Fatigue 2017;98:14–31. https://doi.org/10.1016/j.ijfatigue.2017.01.001.
[10] Pegues JW, Shao S, Shamsaei N, Sanaei N, Fatemi A, Warner DH, et al. Fatigue of additive manufactured Ti-6Al-4V, Part I: The effects of powder feedstock, manufacturing, and post-process conditions on the resulting microstructure and defects. Int J Fatigue 2020;132:105358. https://doi.org/10.1016/j.ijfatigue.2019.105358.
[11] Molaei R, Fatemi A, Sanaei N, Pegues J, Shamsaei N, Shao S, et al. Fatigue of additive manufactured Ti-6Al-4V, Part II: The relationship between microstructure, material cyclic properties, and component performance. Int J Fatigue 2020;132:105363. https://doi.org/10.1016/j.ijfatigue.2019.105363.
[12] Fatemi A, Molaei R, Simsiriwong J, Sanaei N, Pegues J, Torries B, et al. Fatigue behaviour of additive manufactured materials: an overview of some recent experimental studies on Ti-6Al-4V considering various processing and loading direction effects. Fatigue Fract Eng Mater Struct 2019;42:991–1009. https://doi.org/10.1111/ffe.13000.
[13] Nezhadfar PD, Shrestha R, Phan N, Shamsaei N. Fatigue behavior of additively manufactured 17–4 PH stainless steel: synergistic effects of surface roughness and heat treatment. Int J Fatigue 2019;124:188–204. https://doi.org/10.1016/j.ijfatigue.2019.02.039.
[14] Pegues J, Roach M, Scott Williamson R, Shamsaei N. Surface roughness effects on the fatigue strength of additively manufactured Ti-6Al-4V. Int J Fatigue 2018;116:543–52. https://doi.org/10.1016/j.ijfatigue.2018.07.013.
[15] Gockel J, Sheridan L, Koerper B, Whip B. The influence of additive manufacturing processing parameters on surface roughness and fatigue life. Int J Fatigue 2019;124:380–8. https://doi.org/10.1016/j.ijfatigue.2019.03.025.
[16] Zhang J, Fatemi A. Surface roughness effect on multiaxial fatigue behavior of additive manufactured metals and its modeling. Theor Appl Fract Mech 2019;103:102260. https://doi.org/10.1016/j.tafmec.2019.102260.
[17] Gong H, Rafi K, Gu H, Starr T, Stucker B. Analysis of defect generation in Ti-6Al-4V parts made using powder bed fusion additive manufacturing processes. Addit Manuf 2014;1:87–98. https://doi.org/10.1016/j.addma.2014.08.002.
[18] Singh K, Sadeghi F, Correns M, Blass T. A microstructure based approach to model effects of surface roughness on tensile fatigue. Int J Fatigue 2019;129:105229. https://doi.org/10.1016/j.ijfatigue.2019.105229.
[19] Ås SK, Skallerud B, Tveiten BW. Surface roughness characterization for fatigue life predictions using finite element analysis. Int J Fatigue 2008;30:2200–9. https://doi.org/10.1016/j.ijfatigue.2008.05.020.
[20] Romano S, Nezhadfar PD, Shamsaei N, Seifi M, Beretta S. High cycle fatigue behavior and life prediction for additively manufactured 17–4 PH stainless steel: effect of sub-surface porosity and surface roughness. Theor Appl Fract Mech 2020;106. https://doi.org/10.1016/j.tafmec.2020.102477.
[21] Hamidi Nasab M, Romano S, Gastaldi D, Beretta S, Vedani M. Combined effect of surface anomalies and volumetric defects on fatigue assessment of AlSi7Mg fabricated via laser powder bed fusion. Addit Manuf 2019. https://doi.org/10.1016/j.addma.2019.100918.
[22] Solberg K, Guan S, Razavi SMJ, Welo T, Chan KC, Berto F. Fatigue of additively manufactured 316L stainless steel: the influence of porosity and surface roughness. Fatigue Fract Eng Mater Struct 2019;42:2043–52. https://doi.org/10.1111/ffe.13077.
[23] Murakami Y, Tsutsumi K, Fujishima M. Quantitative evaluation of effect of surface roughness on fatigue strength. Nippon Kikai Gakkai Ronbunshu, A Hen/Transactions Jpn Soc Mech Eng Part A 1996;62:1124–31. https://doi.org/10.1299/kikaia.62.1124.
[24] Pegues JW, Shamsaei N, Roach MD, Williamson RS. Fatigue life estimation of additive manufactured parts in the as-built surface condition. Mater Des Process Commun 2019;1:e36https://doi.org/10.1002/mdp2.36.
[25] Vayssette B, Saintier N, Brugger C, El May M, Pessard E. Numerical modelling of surface roughness effect on the fatigue behavior of Ti-6Al-4V obtained by additive manufacturing. Int J Fatigue 2019;123:180–95. https://doi.org/10.1016/j.ijfatigue.2019.02.014.
[26] Masuo H, Tanaka Y, Morokoshi S, Yagura H, Uchida T, Yamamoto Y, et al. Influence of defects, surface roughness and HIP on the fatigue strength of Ti-6Al-4V manufactured by additive manufacturing. Int J Fatigue 2018;117:163–79. https://doi.org/10.1016/j.ijfatigue.2018.07.020.
[27] Wycisk E, Solbach A, Siddique S, Herzog D, Walther F, Emmelmann C. Effects of defects in laser additive manufactured Ti-6Al-4V on fatigue properties. Phys Procedia 2014;56:371–8. https://doi.org/10.1016/j.phpro.2014.08.120.
[28] Uzan NE, Shneck R, Yeheskel O, Frage N. Fatigue of AlSi10Mg specimens fabricated by additive manufacturing selective laser melting (AM-SLM). Mater Sci Eng A 2017;704:229–37. https://doi.org/10.1016/j.msea.2017.08.027.
[29] Spierings AB, Starr TL, Wegener K. Fatigue performance of additive manufactured metallic parts. Rapid Prototyp J 2013;19:88–94. https://doi.org/10.1108/13552541311302932.

[30] Novovic D, Dewes RC, Aspinwall DK, Voice W, Bowen P. The effect of machined topography and integrity on fatigue life. Int J Mach Tools Manuf 2004;44:125–34. https://doi.org/10.1016/j.ijmachtools.2003.10.018.
[31] Greitemeier D, Dalle Donne C, Syassen F, Eufinger J, Melz T. Effect of surface roughness on fatigue performance of additive manufactured Ti–6Al–4V. Mater Sci Technol 2016;32:629–34. https://doi.org/10.1179/1743284715Y.0000000053.
[32] Greitemeier D, Palm F, Syassen F, Melz T. Fatigue performance of additive manufactured TiAl6V4 using electron and laser beam melting. Int J Fatigue 2017;94:211–7. https://doi.org/10.1016/j.ijfatigue.2016.05.001.
[33] Townsend A, Racasan R, Blunt L. Surface-specific additive manufacturing test artefacts. Surf Topogr Metrol Prop 2018;6:024007. https://doi.org/10.1088/2051-672X/aabcaf.
[34] Townsend A, Senin N, Blunt L, Leach RK, Taylor JS. Surface texture metrology for metal additive manufacturing: a review. Precis Eng 2016;46:34–47. https://doi.org/10.1016/j.precisioneng.2016.06.001.
[35] Valente EH, Gundlach C, Christiansen TL, Somers MAJ. Effect of scanning strategy during selective laser melting on surface topography, porosity, and microstructure of additively manufactured Ti-6Al-4V. Appl Sci 2019;9:5554. https://doi.org/10.3390/app9245554.
[36] Franco LA, Sinatora A. 3D surface parameters (ISO 25178–2): Actual meaning of Spk and its relationship to Vmp. Precis Eng 2015;40:106–11. https://doi.org/10.1016/j.precisioneng.2014.10.011.
[37] Edwards P, Ramulu M. Fatigue performance evaluation of selective laser melted Ti-6Al-4V. Mater Sci Eng A 2014;598:327–37. https://doi.org/10.1016/j.msea.2014.01.041.
[38] International Organization for Standardization. ISO 4287:1997. Geometrical product specifications (GPS). Surface texture: profile method. Terms, definitions and surface texture parameters. Geneva; 1997.
[39] Arola D, Williams CL. Estimating the fatigue stress concentration factor of machined surfaces. Int J Fatigue 2002;24:923–30. https://doi.org/10.1016/S0142-1123(02)00012-9.
[40] ASTM International. ASTM E606 standard test method for strain-controlled fatigue testing. West Conshohocken, PA; 2008. p. 1–16. https://doi.org/10.1520/mnl10913m.
[41] Vrancken B, Cain V, Knutsen R, Van Humbeeck J. Residual stress via the contour method in compact tension specimens produced via selective laser melting. Scr Mater 2014;87:29–32. https://doi.org/10.1016/j.scriptamat.2014.05.016.
[42] Wu AS, Brown DW, Kumar M, Gallegos GF, King WE. An experimental investigation into additive manufacturing-induced residual stresses in 316L stainless steel. Metall Mater Trans A Phys Metall Mater Sci 2014;45:6260–70. https://doi.org/10.1007/s11661-014-2549-x.
[43] Chen Z, Wu X, Tomus D, Davies CHJ. Surface roughness of selective laser melted Ti-6Al-4V alloy components. Addit Manuf 2018;21:91–103. https://doi.org/10.1016/j.addma.2018.02.009.
[44] Morrow J. Cyclic plastic strain energy and fatigue of metals. Intern Frict Damp Cycl Plast 1965:45–87. https://doi.org/10.1520/stp43764s.
[45] Ramberg W, Osgood WR. Description of stress-strain curves by three parameters. Nasa Tech Note 1943;902.
[46] Colin J, Fatemi A, Taheri S. Fatigue behavior of stainless steel 304L including strain hardening, prestraining, and mean stress effects. J Eng Mater Technol Trans ASME 2010;132:0210081–02100813. https://doi.org/10.1115/1.4000224.
[47] Colin J, Fatemi A, Taheri S. Cyclic hardening and fatigue behavior of stainless steel 304L. J Mater Sci 2011;46:145–54. https://doi.org/10.1007/s10853-010-4881-x.
[48] Pegues JW, Shao S, Shamsaei N, Schneider JA, Moser RD. Cyclic strain rate effect on martensitic transformation and fatigue behaviour of an austenitic stainless steel. Fatigue Fract Eng Mater Struct 2017;40:2080–91. https://doi.org/10.1111/ffe.12627.
[49] Stephens RI, Fatemi A, Stephens RR, Fuchs HO. Metal fatigue in engineering. 2nd ed. John Wiley & Sons; 2000.
[50] Arola D, Ramulu M. An examination of the effects from surface texture on the strength of fiber reinforced plastics. J Compos Mater 1999;33:102–23. https://doi.org/10.1177/002199839903300201.
[51] Dobrzanski P, Pawlus P. Digital filtering of surface topography: Part I. Separation of one-process surface roughness and waviness by Gaussian convolution, Gaussian regression and spline filters. Precis Eng 2010;34:647–50. https://doi.org/10.1016/j.precisioneng.2009.12.001.
[52] Neuber H. Theory of notch stresses: principles for exact stress calculation. JW Edwards; 1946.
[53] Pegues JW, Roach MD, Shamsaei N. Additive manufacturing of fatigue resistant austenitic stainless steels by understanding process-structure–property relationships. Mater Res Lett 2020;8:8–15. https://doi.org/10.1080/21663831.2019.1678202.
[54] Budynas R, Nisbett JK. Shigley's mechanical engineering design. 11th ed. McGraw-Hill Education; 2015.